



# Microstructure and mechanical properties of an additively manufactured WMoTaNbNiTi refractory high-entropy alloy

Bang Xiao <sup>a,b</sup>, Fangzhou Xing <sup>c</sup>, Wenpeng Jia <sup>a</sup>, Jian Wang <sup>a,\*</sup>, Ming Wei <sup>a,\*\*</sup>, Lian Zhou <sup>a,b</sup>

<sup>a</sup> State Key Laboratory of Porous Metal Materials, Northwest Institute for Non-ferrous Metal Research, Xi'an, Shaanxi, 710016, People's Republic of China

<sup>b</sup> State Key Laboratory of Solidification Processing, Northwestern Polytechnical University, Youyi Western Road, Xi'an, Shaanxi, 710072, People's Republic of China

<sup>c</sup> Thermo-Calc Software AB, Stockholm, Sweden

## ARTICLE INFO

### Keywords:

Selective electron beam melting  
Refractory high-entropy alloy  
Cracking suppression  
Alloying  
High-temperature strength

## ABSTRACT

WMoTaNb refractory high-entropy alloy (RHEA) is pronounced for its brilliant thermal resistance at 1600 °C, which makes it a candidate with vast potential for elevated temperature service except for its difficulty in room temperature machining before industrialization. Additive manufacturing with its complex shape forming and flexible design abilities, can intensively meet the future industrial requirements. However, the additively manufactured WMoTaNb RHEA is restricted by room-temperature brittleness before entering the market. Therefore, we newly developed a WMoTaNbNiTi RHEA, and it has been discovered that Ni, Ti, and Nb at the grain boundaries mainly formed the NiTi B19' phase, thus sharing the residual stresses with the BCC matrix. The ductility of the as-built WMoTaNbNiTi RHEA at room temperature has thus been considerably improved. In addition, an ultimate compressive strength of 738 MPa at 1200 °C was also realized. Consequently, an ideal synergy was achieved between the as-built microstructure, and room- and high-temperature mechanical properties.

## 1. Introduction

Different from the conventional alloy-design methods, high-entropy alloys (HEAs) are prevalent with their vast composition space and flexible composition designs. Hence, elements being used to form HEAs generally consist of light metallic elements, refractory metallic elements, and sometimes nonmetallic elements [1,2]. Among these abovementioned elements, refractory metallic elements are exceptionally and widely accepted in nuclear and aerospace industries [3,4]. In recent years, researchers have preferred to employ refractory elements (see W, Mo, Ta, and Nb) to increase the thermal resistance of HEAs and common titanium alloys [5–10]. The attractive aspects of these refractory elements may somewhat stem from their high-energy barriers. These energy barriers are critical to starting diffusion at elevated and ambient temperatures in alloys dominated by lower melting point elements. However, the previously developed WMoTaNb refractory high-entropy alloy (RHEA), pronounced for its high-temperature superiority, has a critical bottleneck that limits its large-scale industrial applications [11]. Senkov et al. noticed the quasi-cleavage fracture feature and indicated that there exists a ductile to brittle transition temperature

(DBTT) above room temperature [11]. The underlying reasons for the brittleness are mainly owing to a lower strength of the grain boundaries [12] and the intrinsically brittle character of these alloys [13]. However, morphologies of the fracture surfaces of WMoTaNb RHEA suggest a quasi-cleavage fracture mode, which heralds a stronger grain boundary than these cleavage planes (see  $R = \frac{2\gamma_{GBS} - \gamma_{GB}}{2\gamma_{GS}}$ ,  $\gamma_{GBS}$  is the value of the free energy per unit area when forming a new surface at the grain boundary,  $\gamma_{GS}$  is the necessary free energy per unit area in forming new cleavage surface,  $R > 1$  promises a crystal cleavage rather than grain boundary failure) [14]. The lack of ductility also originates from the initial crystal lattice failure before reaching critical shear stress to start dislocation glide [15]. Moreover, the high-entropy, sluggish diffusion, and lattice distortion effects of these RHEAs pose strong barriers to the movement of atoms or other defects [16], which strongly suppress the plastic deformation of this alloy. This indicates that brittleness in alloys such as WMoTaNb RHEA is hard to avoid. Therefore, resolutions to modify the intrinsic brittleness of WMoTaNb RHEA are required to take both grain boundary and intragranular factors into consideration.

To improve the ductility of WMoTaNb RHEA, alloying with appro-

\* Corresponding author.

\*\* Corresponding author.

E-mail addresses: [jwangxjtu@163.com](mailto:jwangxjtu@163.com) (J. Wang), [mingwei\\_mse@sina.com](mailto:mingwei_mse@sina.com) (M. Wei).

priate constituents has been greatly employed [12,17,18]. Naturally, Ti as a widely researched ductile constituent was herein applied to upgrade the microstructure and mechanical properties of WMoTaNb RHEA. This is partly based on the theory that emphasizes decreasing valence electron concentration (*VEC*, e.g.,  $VEC = \sum_{i=1}^N c_i(VEC)_i$ ,  $c_i$  is the atomic percentage of the  $i$ th component), and simultaneously remaining the body-centered cubic (BCC) phase stability of this alloy [17,19,20]. Although Ti can substantially improve the ductility of WMoTaNb RHEA, the overly added amount of it can sometimes damage the high-temperature behaviors. Therefore, trace additions of nonmetallic elements, see carbon and boride, were sequentially realized [12,21,22]. These trace additives have incurred considerable promotion in ductility, mechanical strength, and high-temperature behaviors of WMoTaNb RHEA. However, the diffusion behavior of nonmetallic elements cannot be easily controlled. Local agglomeration of these nonmetallic additives at the grain boundaries can cause intergranular failure when forming brittle phases or particles [23,24]. In contrast, further observations revealed that the segregation of some metallic elements with lower melting points at interdendritic regions or grain boundaries is commonly seen in WMoTaNb-based RHEAs. Moreover, the formation of precipitates or other phases can significantly enhance the matrix of WMoTaNb-based RHEAs [12,25–27]. Above all, it is of great importance to select a room-temperature ductility-withstanding candidate for softening WMoTaNb RHEA, and meanwhile reducing the influence on its high-temperature mechanical properties.

However, limited by their brittleness and hardness, WMoTaNb and WMoTaNb-based RHEAs are confined in applications that essentially accept the as-fabricated components manufactured by these conventional methods, see casting or sparking plasma sintering [11,28–30]. In recent years, some researchers have shown particular interest in the additive manufacturing of RHEAs [31–34]. Considering the deficiency of the conventional methods and the superiority of additive manufacturing in flexible shape preparation under the guidance of a computer-designed model [35]. Studies on additively manufactured WMoTaNb RHEAs are emerging and boosting [36–40].

In the present study, Ni and Ti elements, with their brilliant ductility and high-temperature behaviors, are chosen to play the role of modifying the microstructure and mechanical behavior of WMoTaNb RHEA. Moreover, the significant effects of Ni and Ti additions to WMoTaNb RHEAs were also verified in previous studies [17,19,32,41,42]. When considering these constituent parts in WMoTaNb RHEA, it can be noted that the W element has a ductile to brittle transition temperature (DBTT) above 350 °C, whereas WTa-formed alloys have a DBTT of approximately 900 °C [43,44]. For these reasons, some researchers tried to remove W from WMoTaNb RHEA and designed new refractory alloys with considerable room temperature behaviors [45,46]. However, W, Mo, and Ta dominate the high-temperature superiority. Therefore, based on the Ni and Ti additions, we also choose to decrease Ta addition and increase Mo content (for its outstanding additive manufacturing formability and mechanical behaviors at high temperatures) [47–49]. Selective electron beam melting (SEBM), with its high-energy electron beam, preheating of powders, and post-thermal compensation, is capable of improving the printability of WMoTaNbNiTi RHEA under such large solidification and cooling ranges between W (3410 °C), Ni (1453 °C), and room temperature [34]. Moreover, a very wide range of moving-electron-beam speeds to choose from in combination with the highly controlled vacuum atmosphere makes the SEBM process eminently suited for fabricating complex structures. To achieve reliable microstructures paced by these fully covered processing parameters in SEBM processes, a widened linear energy density range was selected. Further investigation attempts to develop a whole picture of the morphology, distribution, and effects of the alloying elements in the microstructures as well as the mechanical properties of the as-built WMoTaNbNiTi RHEAs. The systematic study on processing parameters and alloying effects influenced microstructure evolution, phase

constituents, and mechanical properties of the as-built WMoTaNbNiTi RHEAs will trigger a new insight into WMoTaNb RHEAs.

## 2. Experimental procedures

### 2.1. Composition design

Combined with the initial idea of compositional design (see in the last paragraph of Introduction) for ductilizing and microstructure optimization of WMoTaNb RHEA during additive manufacturing, a suitable calculation (calculated by Thermo-Calc software with database HEA6) of the evolution of alloy concentration by Scheil solidification of W, Mo, Ta, Nb, Ni, and Ti in liquid and solid at different temperatures are presented in Fig. 1. It can be noted that contents of W and Mo decrease significantly at the initial stage of solidification. Ni, Ti, and Nb are highly concentrated at the stage near their melting points, which hints a NiTiNb condensation at the last solidification stage, simultaneously, there is a clear increasing tendency of Ta content. It can be noted that Ni and Ti can be segregated to the last solidified sites, see grain boundaries or interdendritic regions, according to Scheil solidification mode ( $c_s = kc_0(1 - f_s)^{k-1}$ ,  $c_0$  is the initial liquid composition,  $k = c_s/c_l$ ,  $c_l$  or  $c_s$  is the concentration of the solid or liquid at the solid/liquid interface,  $f_s$  denotes the fraction of the solid).

### 2.2. Raw materials

The commercially available W, Mo, Ta, Nb, Ni, and Ti powders have a purity of over 99.5 wt%, and all these powders were physically blended for 8 h in a sealed metal jar. The atomic ratio of the constituent powders is W: Mo: Ta: Nb: Ni: Ti = 20: 42: 14: 19: 2.5: 2.5. In these powders, W, Mo, Ta, and Nb are fabricated by plasma rotating electrode processing (PREP) with highly spherical diameters confined within 50 μm. Ni and Ti nonspherical powders having particles in diameters limited to 100 μm were prepared using gas (Ar) atomization (GA). Ni and Ti have lower melting points compared to W, Mo, Ta, and Nb, herein it is reasonable to choose coarse powders (less exposed area under electron beam compared to fine powders under the same weight) with large particle sizes in case of severe vaporization during SEBM processing [40,50]. The as-mixed WMoTaNbNiTi powder is shown below in Fig. 2.

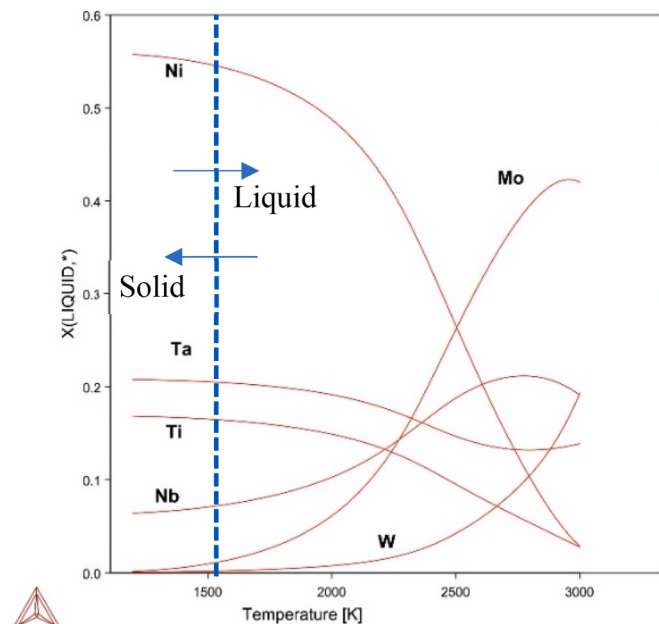
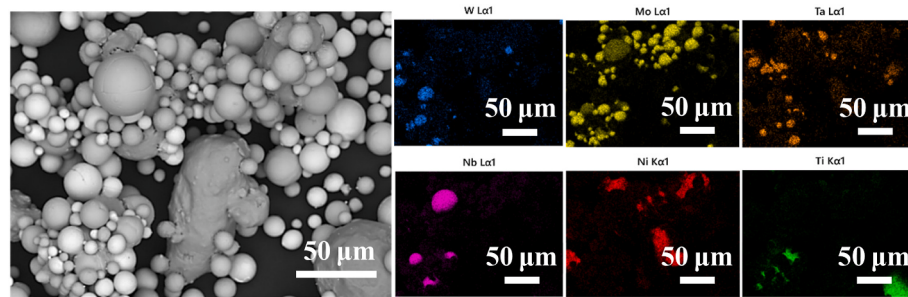


Fig. 1. Liquid content-temperature evolution.



**Fig. 2.** Morphologies of (a) the as-mixed powder and distribution of W, Mo, Ta, Nb, Ni, and Ti constituents.

### 2.3. Sample preparation

The as-mixed WMoTaNbNiTi powder was melted, then formed WMoTaNbNiTi RHEAs using a SEBM facility (Xi'an Sailong Metal Materials Co., Ltd.) on the molybdenum substrate with a working voltage of 60 kV, a scanning current of 18 mA, and a variety of scanning rates of 0.3 m/s, 0.5 m/s, 0.7 m/s, 0.9 m/s, 1.1 m/s, and 1.3 m/s, respectively. Before SEBM processing, the substrate was preheated to 1100 °C, after the beginning of SEBM processing, the temperature of the substrate remained stable at a temperature range above 850 °C. A schematic diagram of the simplified SEBM processing and the as-built WMoTaNbNiTi RHEAs is shown in Fig. 3. It is noticeable that the as-built WMoTaNbNiTi RHEAs were formed in a sealed environment under a vacuum of  $10^{-1}$  Pa and the dimension of all the as-built RHEAs is length × width × height = 15 mm × 15 mm × 10 mm. The density of the as-built WMoTaNbNiTi RHEAs was measured according to the standard Archimedes' method. The weights of the samples were measured to be greater than 15 g with an accuracy of  $\pm 0.0001$  g.

### 2.4. Materials characterization

Crystal structure and phase constituents of the as-built WMoTaNbNiTi RHEAs were displayed using X-ray diffraction (XRD, Brucker D8 ADVANCE) patterns with a CuK $\alpha$  source, a step size of 0.02°, and a scanning range of 20–100°. The as-built WMoTaNbNiTi RHEAs were all

sliced into two pieces along the build direction. Subsequent grinding and polishing of the as-cut surfaces were completed using abrasive papers (with silicon carbide or SiC particles, successively using 150-mesh, 500-mesh, and 1000-mesh abrasive papers) and thin silk polishing cloth. Microstructures of the as-polished lateral surfaces (parallel to the build direction) and fracture surfaces of the as-built WMoTaNbNiTi RHEAs samples (refer to fracture surfaces of samples experienced compression tests, see part 2.5) were carried out using scanning electron microscopy (SEM, JEOL JSM-IT500LA) with an energy dispersive X-ray spectroscopy (EDX) operating at an acceleration voltage of 20 kV. The microstructures, crystal structures, and phase distribution inside the as-built WMoTaNbNiTi RHEAs were characterized using the high-resolution transmission electron microscopy (HRTEM, JEOL JEM-2100Plus) at an operation voltage of 200 kV, in conjunction with an EDX system. Before the HRTEM characterization, a thin foil was prepared by a precision ion milling system (Ganta-610C) for about 7 h until it was applicable for transmission electron.

### 2.5. Mechanical tests

Hardness was tested on the as-polished lateral surfaces of the samples using a Vickers Hardness Tester (Mitutoyo HM-200) with an applied load of 200 gf and a hold time of 15 s. At least seven randomly selected locations of every sample were tested. The room temperature compression test of the as-built WMoTaNbNiTi RHEAs was carried out

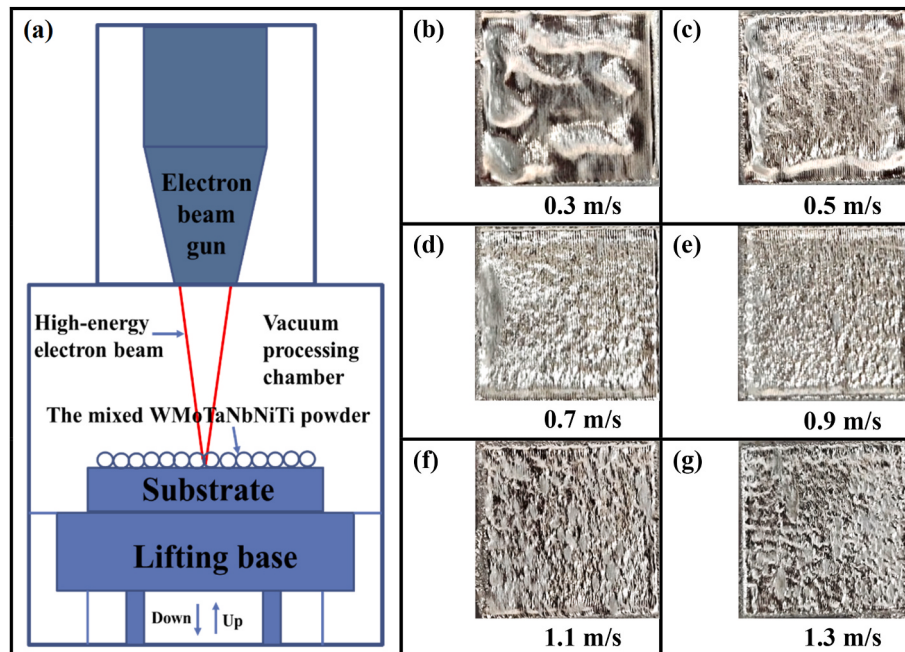


**Fig. 3.** The simplified schematic diagram of the SEBM processing (a) and surface morphologies of the as-built WMoTaNbNiTi RHEAs at scanning rates at (b) 0.3 m/s; (c) 0.5 m/s; (d) 0.7 m/s; (e) 0.9 m/s; (f) 1.1 m/s; (g) 1.3 m/s.

on an INSTRON 5985 testing machine at a constant strain rate of  $10^{-3}/\text{s}$ . All the samples (with their axis along the build direction) prepared for the compression test were 4 mm in diameter and 6 mm in height. Before carrying out the compression test, these samples were ground using abrasive papers (1000 mesh and 2000 mesh). Pillars sliced from the as-built WMoTaNbNiTi RHEAs formed at different scanning rates (see 0.3 m/s, 0.5 m/s, 0.7 m/s, 0.9 m/s, 1.1 m/s, and 1.3 m/s, respectively) were compressed to obtain the strength values. Moreover, the selected samples were heated to the operating temperature for 45–60 min and soaked at temperature for 15 min under 5 N load control, compression test was performed using the facility (DOLI DDL200) at 1200 °C under Ar atmosphere with a constant strain rate of  $10^{-3}/\text{s}$ . Nanoindentation test (Fig. 4,  $h_r$  is the residual penetration depth after unloading,  $h_{\max}$  is the maximum depth where the indenter tip reached) for the chosen polished lateral surface of the as-built WMoTaNbNiTi RHEAs was performed on a nanoindenter (TI 950 TribolIndenter, HYSITRON) with a Berkovich indenter at room temperature. At least seven testing sites were randomly measured. The peak stress of the indenter tip was chosen to be 9000  $\mu\text{N}$ , the loading rate was 1800  $\mu\text{N}/\text{s}$ , and the duration time of the testing process was 5 s.

### 3. Results

#### 3.1. Printability

SEBM, equipped with the focused high-energy electron beam, completely melted the mixed WMoTaNbNiTi powder (see Fig. 3(a)). Values of the density of these as-built RHEAs formed at scanning rates of 0.3 m/s, 0.5 m/s, 0.7 m/s, 0.9 m/s, 1.1 m/s, and, 1.3 m/s are 12.35 g/cm<sup>3</sup>, 12.56 g/cm<sup>3</sup>, 12.47 g/cm<sup>3</sup>, 12.50 g/cm<sup>3</sup>, 12.36 g/cm<sup>3</sup>, and, 12.31 g/cm<sup>3</sup>, respectively, and are smaller than that of the as-cast WMoTaNb RHEA [28]. The as-built WMoTaNbNiTi RHEAs appeared in Fig. 3(b)–(d) exhibit different surface conditions. It can be seen that increasing scanning rates or decreasing heat input has a significant influence on the as-built microstructures. To clarify the microstructure evolution, linear energy density ( $E_l = \eta \frac{P}{v}$ ,  $\eta$  is constant,  $P$  is power (J/s),  $v$  is scanning rate (m/s)) is employed to relate microstructure variations to processing parameters [51,52]. Because the SEBM process is accomplished inside a vacuum environment, thus  $\eta$  approaches 1. The calculated  $E_l$  values (Fig. 5) for WMoTaNbNiTi RHEAs are 3600 J/m, 2160 J/m, 1543 J/m, 1200 J/m, 982 J/m, and 831 J/m, respectively. It has been hinted that varying processing parameters, such as scanning rate, can substantially influence the microstructures [33,40]. The surface morphologies of the as-built WMoTaNbNiTi RHEAs in Fig. 3(b)–(d) present microstructure evolution from over-melted state (Particular in Fig. 3(b)) to a little incompletely-fused surface condition (Fig. 3(g)). The calculated energy density differences, see  $\Delta E_1$  and  $\Delta E_2$ , promise two separate microstructure evolution trends. Microstructures formed at scanning rates of 0.3 m/s, 0.5 m/s, and 0.7 m/s exhibit a drastic evolution, whereas microstructures formed at 0.9 m/s, 1.1 m/s, and 1.3 m/s evolved peacefully (see Fig. 3(b)–(g)).

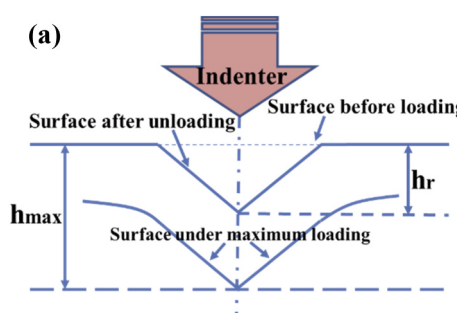


Fig. 4. Schematic diagram of nanoindentation test (a) and (b) indentation.

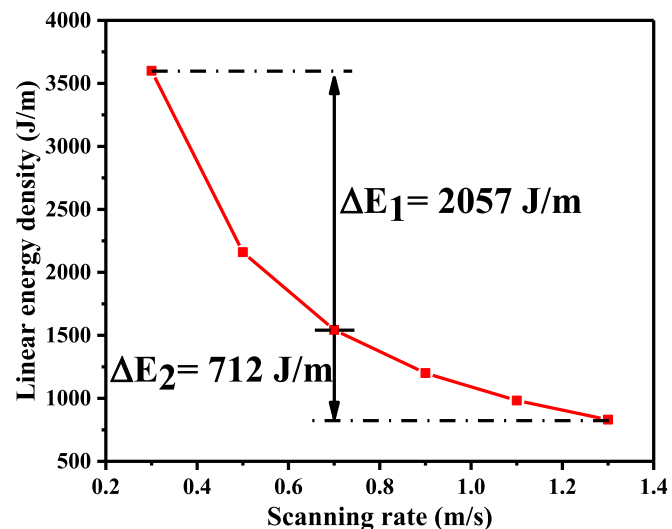
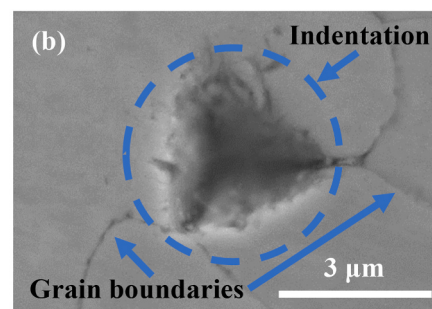


Fig. 5. Linear energy density at different scanning rates.

The as-polished lateral microstructures along the build direction of the as-built WMoTaNbNiTi RHEAs are shown in Fig. 6. It can be noticed that the as-polished surfaces in Fig. 6(a)–(f) exhibit fewer short cracks, small pores, and some incompletely fused regions as the linear energy density changes. It can be confirmed that the microstructures of the as-built WMoTaNbNiTi RHEAs have been substantially improved in quality [36–38].

Solidification cracking or hot cracking is a serious defect, which is commonly encountered in welds, casting, and additive manufacturing processes [35,39]. It can also occur in the additively manufactured WMoTaNb or WMoTaNb-based RHEAs about the large solidification range, the strain caused by rapid cooling, solidification shrinkage, and thermal contraction. On the contrary, constituents with lower melting points can play a bridging role to supply feeding flow for cracking suppression [39,40]. Secondary electron and backscatter modes in Fig. 7 (a) and (b) present a grain surrounded by an inhomogeneous grain boundary with segregation, and W, Mo, and Ta elements constructed the main body of the grain, whereas lower melting points elements, such as Nb, Ni, and Ti distributed in the space of grain boundaries.

Research on NiTi alloys put forward the superelasticity behavior which intrinsically originates from a stress-induced austenite→R-phase→B1' martensite transformation [53,54]. Furthermore, in-depth research explored the extended superelasticity of NiTiNb alloy and its shape memory character [55,56]. Subsequently, a W–NiTiNb alloy without brittle intermetallics was developed and showed excellent compressive strength and ductility (see Fig. 4 in Ref. [57]). Therefore, it is natural to correlate the cracking-relief phenomenon in the as-built WMoTaNbNiTi RHEAs to the thermal shock resistance of NiTiNb segregation at the grain boundaries [58,59]. Moreover, NiTiNb alloys have been successfully manufactured using selective laser melting,



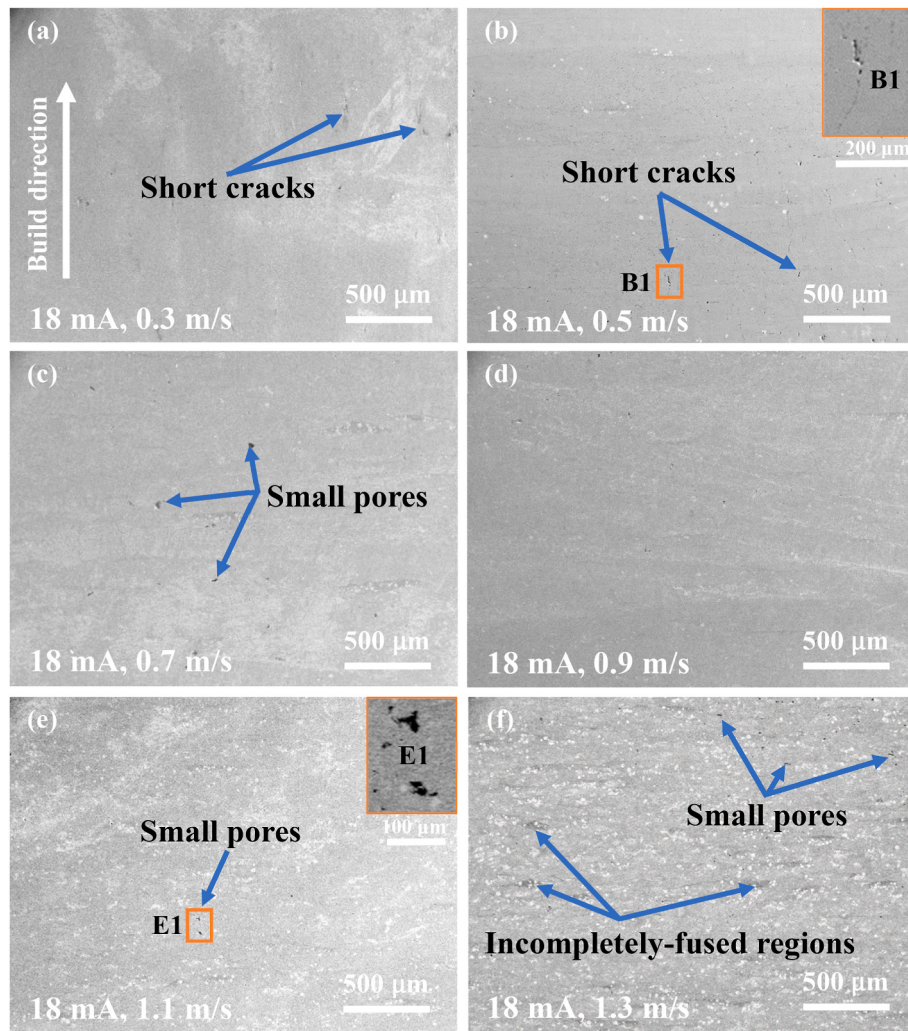


**Fig. 6.** Microstructures of the as-built WMoTaNbNiTi RHEAs formed at different scanning rates of (a) 0.3 m/s, (b) 0.5 m/s, (c) 0.7 m/s, (d) 0.9 m/s, (e) 1.1 m/s, (f) 1.3 m/s.

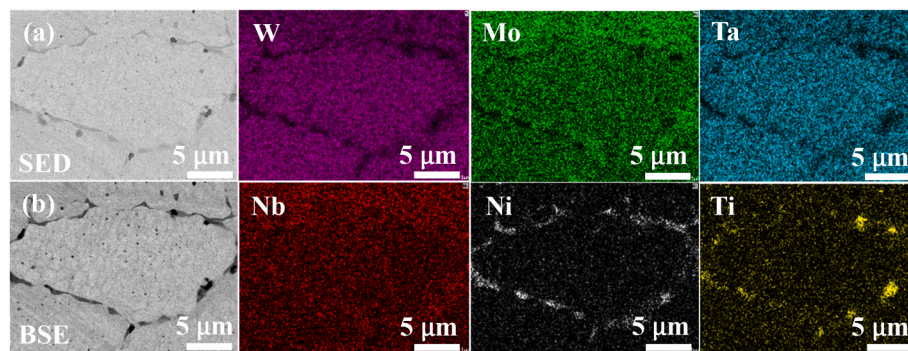


**Fig. 7.** Microstructure under (a) secondary electron mode, (b) backscatter electron mode, and the elemental distribution of the as-built WMoTaNbNiTi RHEA.

which highly testified to the stability of NiTiNb-rich grain boundaries when tirelessly confronting thermal cycles [60].

### 3.2. Phase constituents

To fully understand the microstructures and phase constituents of the as-built RHEAs, XRD was performed (Fig. 8). The as-built WMo-TaNbNiTi RHEAs formed at different scanning rates consist of a primary BCC phase, FCC phase, and NiTi (Fig. 8). It can be noticed that when

increasing the scanning rate, intensity of NiTi peaks (see peaks intensity variation at  $2\theta$  near  $40.2^\circ$  and  $63.5^\circ$ ) increases simultaneously. This indicates a decreasing trend in the vaporization of Ni and Ti elements [40,61] caused by decreasing linear energy density (Fig. 5).

The detailed phase constituents were sequentially displayed using TEM and EDX mapping. Fig. 9 shows two different types of NiTi (B19' phase and Ni-Ti segregation) at the grain boundaries of the primary BCC phase. This means NiTi, in nanoscale size, has at least two types of existing forms, for instance, precipitation and micro-segregation. In

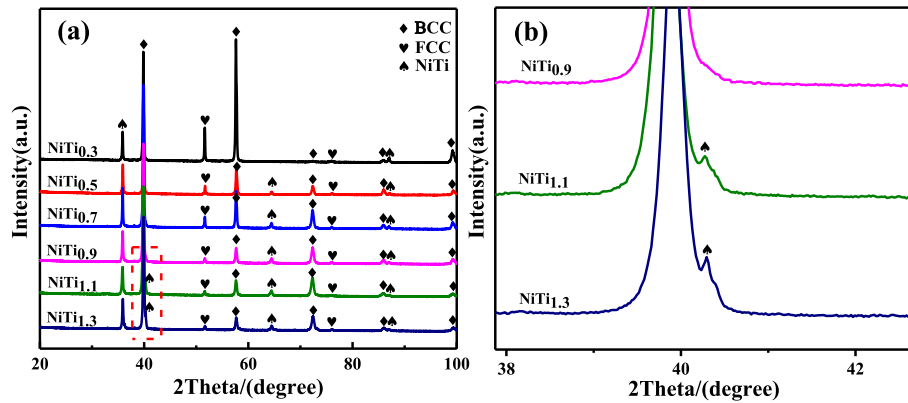


**Fig. 8.** RD patterns of the as-built WMoTaNbNiTi RHEAs (a) and (b) local sites of (a) under higher magnification (NiTi<sub>0.3</sub> represents the as-built WMoTaNbNiTi RHEA formed at a scanning rate of 0.3 m/s, others (form NiTi<sub>0.5</sub> to NiTi<sub>1.3</sub>) are similar to this).

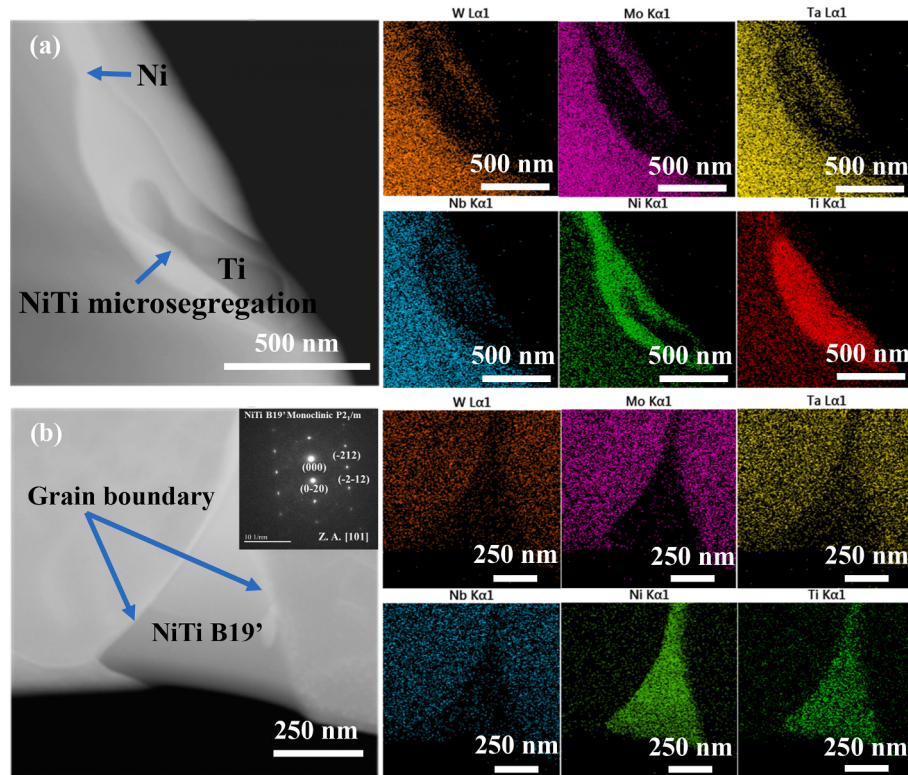


**Fig. 9.** (a) NiTi, Ni, and Ti at grain boundaries and (b) NiTi.

**Fig. 9(a)**, Ti is located in the central place of the Ni–Ti-rich region. It is worth noting that there is a sequence of Ti (melting point, 1668 °C)→NiTi (melting point<1453 °C)→Ni (melting point, 1453 °C) from internal to outside. This reflects the occurrence of solidification of Ni and Ti in this micro-sized region [62]. Because of the high melting points of W, Mo, Ta, and Nb, the matrix formed above 1700 °C, thus separating Ti- and Ni-rich fluid (Figs. 7 and 9). When the temperature dropped to the range near the melting points of Ti, it began to solidify. The rapid cooling rates in the as-built WMoTaNbNiTi RHEAs accelerated the solidification process, thus maintaining the residual NiTi at room temperature and avoiding being separated into two phases (see pure Ti and Ni). This Ni, Ti, and NiTi assembly in **Fig. 9(b)** strongly support the Ni, Ti liquid feeding to the grain boundary, and formation of NiTi micro-alloying (**Fig. 9(a)**). Moreover, the only FCC phase in the micro-structure that has been observed is Ni at the grain boundary in **Fig. 9(a)**, which decreases with the increase of scanning rates. Therefore, it can be

deduced that the FCC phase (Ni) also plays a role in liquid feeding at the grain boundary and helps decrease crack susceptibility.

### 3.3. Mechanical properties

The engineering stress-strain curves of WMoTaNbNiTi RHEAs formed at electron beam scanning rates ranging from 0.3 m/s to 1.3 m/s are presented in **Fig. 10(a)**. The main concern for WMoTaNb and WMoTaNb-based RHEAs is their impressively poor ductility at room temperature [11]. In contrast, all these samples presented in this study exhibit considerable compressive ductility at ambient temperature. The strength and deformation before fracture (DBF) initially display an increasing tendency and reach the highest point at a scanning rate of 1.1 m/s. The as-built RHEA at a scanning rate of 1.1 m/s has a compressive yield strength of above 1500 MPa and an ultimate compressive strength (UCS) of 2085 MPa while having a DBF of 21.76 %. In detail, apart from

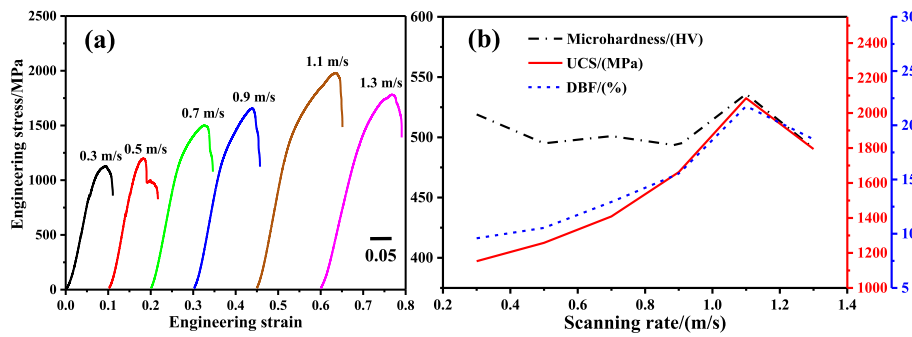


Fig. 10. Engineering stress-strain curves (a) and variation tendencies of the hardness, UCS, and DBF of the as-built WMoTaNbNiTi RHEAs.

the elastic stage, there is still a ductility of the as-built WMoTaNbNiTi RHEA at a scanning rate of 1.1 m/s of >10 %. The mechanical properties of the as-built WMoTaNbNiTi RHEAs formed at different scanning rates are summarized in Fig. 10(b). Notably, the hardness, UCS, and DBF of the as-built WMoTaNbNiTi RHEAs show similar changing tendencies as the scanning rate increases. The hardness values reached the highest point (536 HV, Table 1) at a scanning rate of 1.1 m/s.

In Refs. [11,28], WMoTaNb RHEA has the hardness, compressive yield strength, UCS, and ductility of 460 HV, 1058 MPa, 1211 MPa, and 2.1 %, respectively. Compared to these previously conducted researches, it is obvious that the mechanical properties herein possess a considerable improvement. The elastic modulus of the as-built WMoTaNbNiTi RHEA at a scanning rate of 1.1 m/s is  $240 \pm 7$  GPa, a little higher than  $220 \pm 20$  GPa of WMoTaNb RHEA [11]. Results of the nanoindentation experiment show a measured maximum depth ( $h_{\max}$ ) of  $145 \pm 6$  nm, a residual depth ( $h_r$ ) of  $97 \pm 9$  nm after unloading, and a nanoscale ductility of  $0.67 \pm 0.09$ , which promises better local coordination in deformation of adjacent regions near grain boundaries. In addition, all the as-built WMoTaNbNiTi RHEAs have a significant steady-state strain hardening before approaching UCS or even fracture with a strain-hardening coefficient of the engineering stress-strain curves ( $\gamma = \Delta\sigma/\Delta\delta$ ,  $\delta$  denotes the ductility) which is estimated to be 5.17 GPa.

The engineering stress-strain curve of compression test at 1200 °C suggests an excellent thermal resistance of the as-built WMoTaNbNiTi RHEA formed at scanning rate of 1.1 m/s (see Fig. 11). The UCS and DBF of the as-built WMoTaNbNiTi RHEA are 738 MPa and 17.4 % (UCS in work of WMoTaNb RHEA by Senkov and coworkers [11] at 1200 °C is 803 MPa). These results clarified that the addition of Ni, and Ti elements improved the mechanical behavior of the as-built WMoTaNbNiTi RHEA and remained a considerable thermal resistance of this RHEA.

## 4. Discussion

### 4.1. Printability

NiTi and NiTiNb alloys have already been researched in numerous papers for their impressive superelasticity [42,57,59]. Moreover, additively manufactured NiTi and W–NiTiNb alloys exhibit excellent mechanical behaviors [57,59,60,63]. However, the residual thermal stresses in the additively manufactured alloys during melting processes can reach 300–400 MPa [64,65]. In Fig. 7, Ni, Ti, and Nb segregation at grain boundaries can substantially enhance the bonding between grains, and ameliorate deformation inconsistency between adjacent grains or

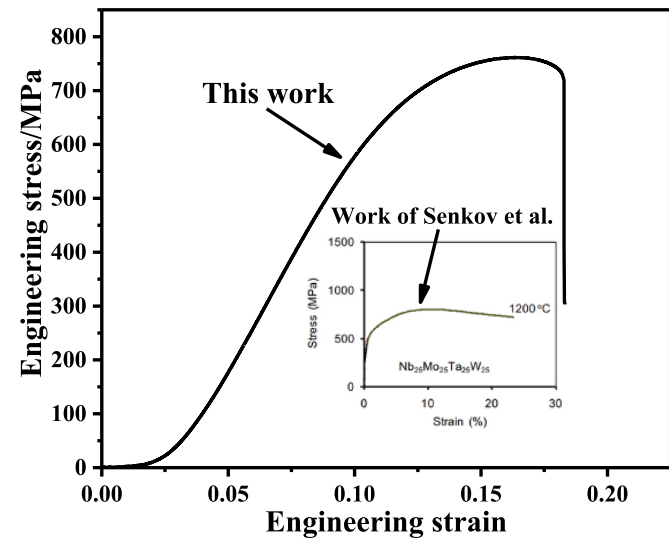


Fig. 11. Engineering stress-strain curves of the as-built WMoTaNbNiTi RHEA and the as-cast WMoTaNb RHEA [11] compressed at 1200 °C.

phases by releasing thermal stresses provoked by large thermal gradients and thermal cycles.

After SEBM of the as-built WMoTaNbNiTi RHEAs, there was still a post-heating process, which kept the temperature of the substrate above 850 °C. The post-heat treatment and grain boundary strengthening of NiTi and NiTiNb constituents lowered the undesirable cracking susceptibility by sharing loads caused by residual stresses during this large cooling temperature range [66,67].

Besides, there are also some dislocations in the as-built WMoTaNbNiTi RHEAs, which might glide, climb, and move on not well-defined crystallographic planes (similar to that displayed in Fig. 26.15 (A) in Ref. [68]) during the cooling stage after SEBM (Fig. 12(a)). Dislocations in WMoTaNbNiTi RHEAs glided from the matrix to the precipitates and agglomerated at the phase boundary (Fig. 12(b)). This phenomenon somewhat demonstrates the occurrence of stress-sharing between the BCC matrix and precipitates. In addition, dislocations constructed cellular substructures (Fig. 12(c)), or similar substructures (see Fig. 12 in Ref. [69], Fig. 10(i) and (k) in Ref. [70], and Fig. 15 in Ref. [71]) are frequently generated in alloys that experienced or are experiencing a high-temperature process [72]. During SEBM of WMoTaNbNiTi RHEAs, thermal cycles enforced dislocations rearranged to stay at a lower energy configuration, which somewhat indicates a route for remitting impact from cyclic thermal stresses, thus decreasing cracking susceptibility [73]. Moreover, there is a (Ta, Nb, Ni, Ti)-rich particle (which correlates well with the calculated result shown in Fig. 1 and also agrees well with the calculation of phase diagrams in Refs. [32,74]) in Fig. 12(d) with deformed surface. In the meantime,

**Table 1**  
Mechanical properties of the as-built WMoTaNbNiTi RHEAs.

Scanning rate/(m/s)	0.3	0.5	0.7	0.9	1.1	1.3
Hardness/(HV)	519	495	501	493	536	491
UCS/(MPa)	1153	1258	1409	1662	2085	1794
DBF	9.58	10.54	12.93	15.53	21.76	18.71

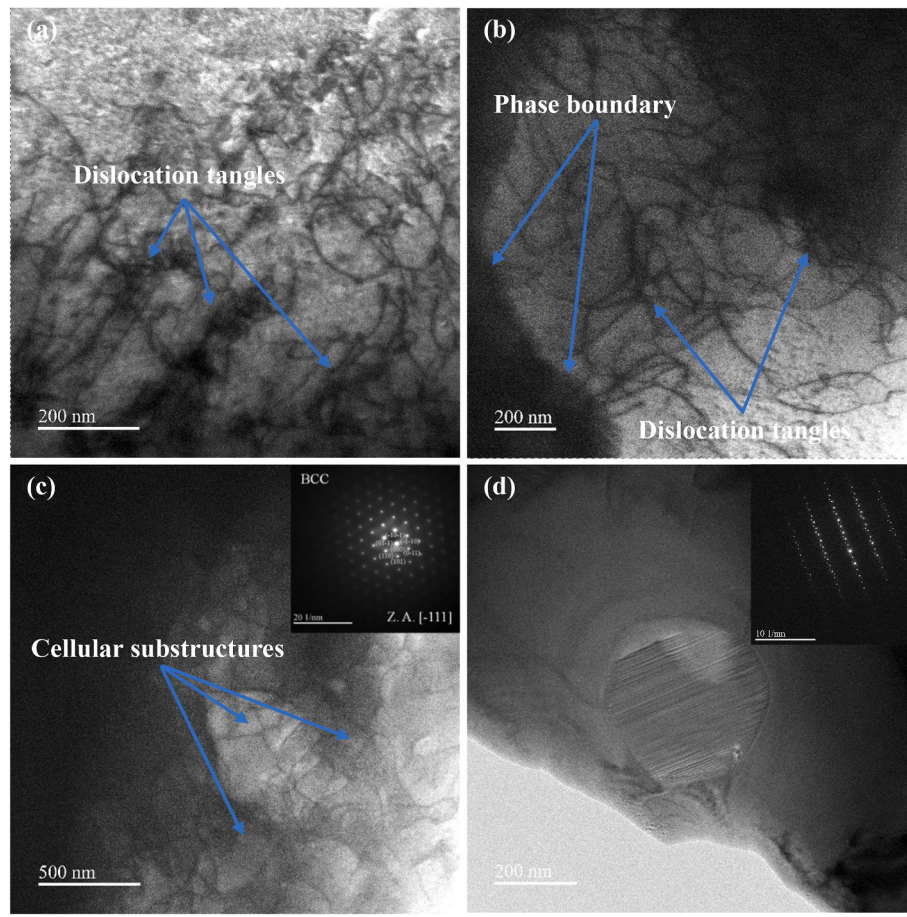


**Fig. 12.** Dislocations in the BCC matrix (a); (b) dislocation campaign between phases; (c) cellular structures; (d) deformation of NiTiNb particles.

dislocations have been substantially reduced in regions adjacent to this (Ta, Nb, Ni, Ti)-rich particle. Therefore, it can be taken for granted that the formation of this serious deformed structure (sometimes stacking fault) in Ni-constituted alloys [32,68,75,76] can be another way to alleviate residual stresses in the as-built WMoTaNbNiTi RHEAs. Furthermore, the temperature preheated up to 1100 °C and the stable temperature preservation above 850 °C during the whole melting process have helped ensure a lowered cracking susceptibility in the as-built WMoTaNbNiTi RHEAs [77].

#### 4.2. Strengthening mechanism

The lower the linear energy density values, the smaller and shallower the melting pool sizes, as well as the lower the thermal gradients. In detail, a smaller and shallower melting pool induces fewer heat-affected areas, which thus promises lower thermal gradients and a more rapid cooling rate, leading to fewer chances for grain growth. Meanwhile, the reduction of vaporized amounts of these elements, e.g., Nb, Ni, and Ti, caused by the dropping linear energy density values can effectively accelerate the generation of more precipitates (this will be discussed later), and eventually contribute to a stronger solid-solution strengthening effect [50,78]. However, lower linear energy density produced some visible incompletely-fused W particles, which to some degree damaged the solid-solution strengthening effect with less W solute in the matrix (see Fig. 6(f) and Fig. 10(a)).

In Fig. 12(a), dislocations (screw or nonscrew dislocations, see Fig. 3 (a) in Ref. [79]) are densely generated in the as-built WMoTaNbNiTi RHEAs. These densely distributed dislocations tangled together to perform barriers for precluding other dislocations from gliding in the matrix. Furthermore, it can be noticed that dislocations in the BCC

matrix also glide to the phase boundaries, whereas phase boundaries prevent dislocations from crossing these obstacles. Therefore, dislocation-phase boundary interactions form dislocations tangles, pile-ups, or forest dislocations, which as impediments hinder these moving dislocations by lessening their mean free path, causing dislocation locking together and strengthening the as-built WMoTaNbNiTi RHEAs. Detailed observation shows a clear phase boundary between the (Ta, Nb, Ni)-rich particle, hence deformation of the (Ta, Nb, Ni, Ti)-rich particle calls for more dislocations (Fig. 13) or dislocation pile-ups to guarantee. It has been confirmed that the cellular substructures can significantly improve the strength of the additively manufactured alloys through trapping and retaining dislocations and suppressing twinning [80–82]. Additionally, the formation of the cellular substructures in the as-fabricated microstructures of WMoTaNbNiTi RHEAs by thermal cycles caused stresses during SEBM played an important role in suppressing these dislocations from moving away and supplying nucleation sites for dislocation loops, thus leading to more serious dislocation interactions, finally enhancing the strength of the as-built RHEAs during deformation [83–85]. Likewise, precipitation in the as-built WMoTaNbNiTi RHEAs also played a role of paramount importance. In Fig. 14 (a), the TEM image presents some precipitated NiTi particles (B19', monoclinic, P2<sub>1</sub>/m) in the matrix. A higher magnification image reveals the retardment of dislocations posed by these particles (Fig. 14(b)). Energy consumption of dislocations in overcoming these particles by crossing and leaving dislocation loops contributes to the deformation resistance of the metal matrix. Last, but not least, the rapid cooling rates and Ni-Ti alloying effect added severe lattice distortion to the as-printed metastable BCC matrix, see the resulting precipitates by over-saturated solution after SEBM, which positively enhanced the barrier to the moving dislocations in the crystal lattices [86,87]. In summary, these

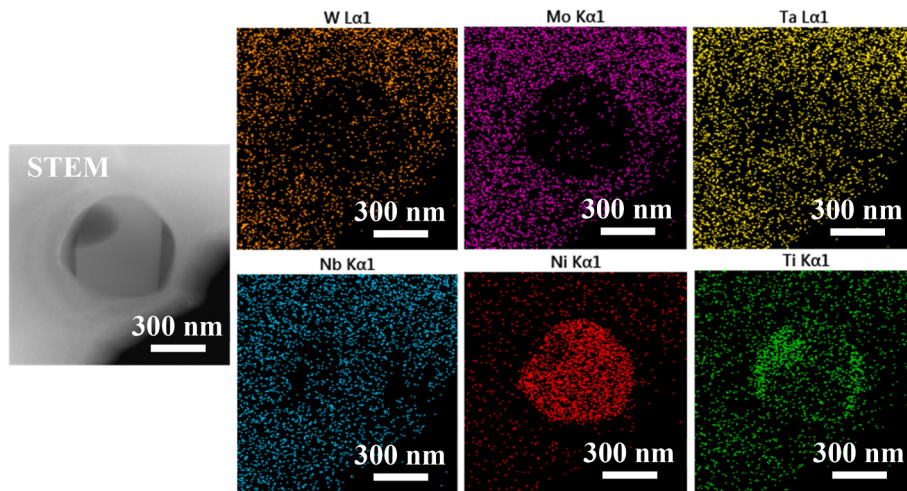


**Fig. 13.** Elemental distribution of particles in the as-built WMoTaNbNiTi alloy.

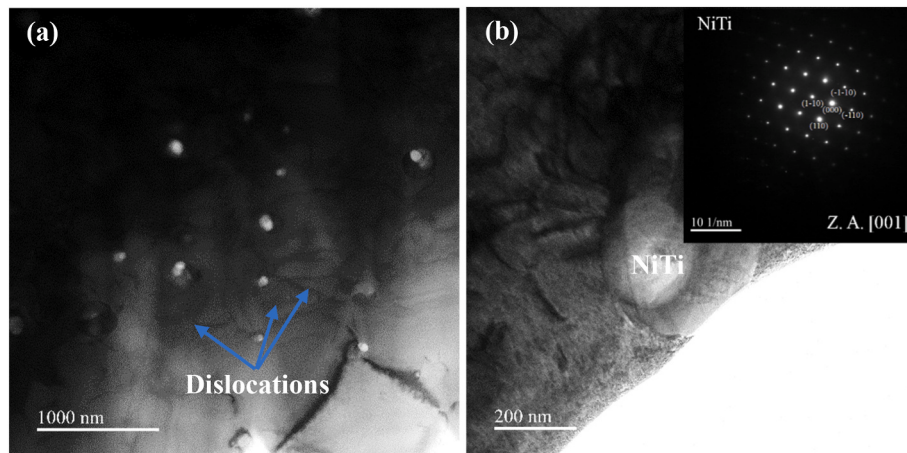


**Fig. 14.** NiTi particles (a)(b) in the as-built WMoTaNbNiTi RHEAs.

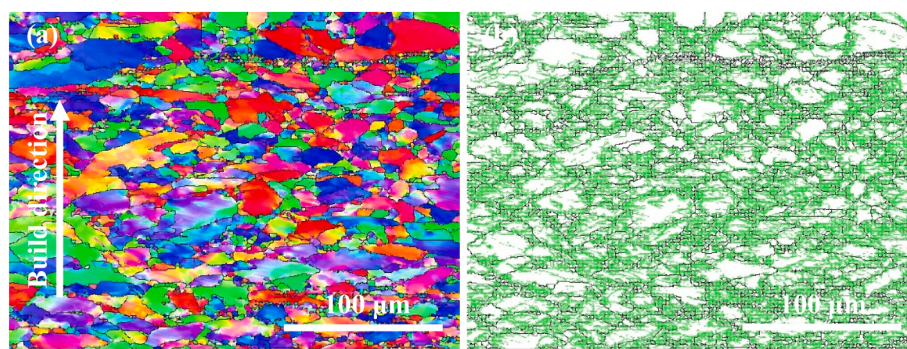


**Fig. 15.** The as-deformed microstructure of the as-built WMoTaNbNiTi RHEA at 1200 °C (a) inverse pole figure and (b) grain boundaries.

dislocation pile-ups, dislocation tangles, and precipitates induced retardment to dislocation movement [88,89]. The cellular-substructures-controlled glide of dislocations within the matrix [90,91], and the primary solid-solution strengthening mechanism naturally reinforced the matrix and resultantly aggravated the work-hardening in the as-built WMoTaNbNiTi RHEAs (Fig. 10(a)).

The ductility of the as-built WMoTaNbNiTi RHEAs is mainly improved by using Nb, Ni, and Ti to modify the cohesion between grain boundaries. In Fig. 15(a) and (b), the as-deformed microstructure

suggests equiaxed grains in the as-deformed WMoTaNbNiTi RHEA with dense substructures populated at grain boundaries. Therefore, dislocations can impinge upon and pile up in regions adjacent to the grain boundaries [92,93], and reorient within and cross the grain boundaries, thereby propagating slip into another grain [94,95]. In Fig. 7, NiTiNb segregation at the grain boundaries can substantially enhance the deformation coordination between neighboring grains. This is similar to the stress-relief mechanism in B-doped Ni<sub>3</sub>Al by slip transmission of dislocations to the adjoining grains, thus mitigating the nucleation and

propagation of cracks along the grain boundary during deformation [96]. It has also been researched that aggregation of chemical disordering at grain boundaries can sometimes enhance the ductility of materials [97,98]. Thus, continuous deformation between grains and the grain boundary phases (Nb, Ni, Ti-rich regions, NiTi, and NbNiTi phases) can considerably extend the mean free path of dislocations during slipping. Besides, deformation of the (Ta, Nb, Ni, Ti)-rich particle consumed some dislocations by generating serious lattice distortion, which promises a new way for ductility improvement of the as-built WMoTaNbNiTi RHEAs [75,76]. The segregation or precipitation of NiTi can also provide places for dislocations to glide on, that is to say, precipitation and segregation of NiTi extended the mean free path of dislocations, hence increasing the ductility [19,99–101]. Moreover, the SEBM process, as a processing method itself can induce high-density dislocations (Fig. 12(a) and (b)) with thermal variables near or inside the melt pool [102], sometimes in the form of geometrically necessary dislocations to accommodate the heterogeneous deformation between adjacent phases or grains [79]. Furthermore, dislocations as a main part of the ductile materials activate a longer plastic deformation in the as-built WMoTaNbNiTi RHEA (Fig. 10).

## 5. Conclusion

In summary, Ni and Ti additions in WMoTaNb RHEA played an important role in enhancing cohesion between the grain boundaries. Moreover, there are high-density dislocations appeared in the currently studied BCC matrix of the as-built WMoTaNbNiTi RHEA. Tangles, agglomeration of dislocations at the phase boundaries, and precipitation (NiTi particles) caused retardments to these moving dislocations, resulting in the strengthening of the metal matrix. Improvement of the ductility of the as-built WMoTaNbNiTi RHEAs depends mainly on dislocation glide, the NiTi precipitates in the BCC matrix can substantially enlarge the mean free path of dislocations, thus ductilizing the as-built WMoTaNbNiTi RHEAs. The synergy between microstructure, strength, and ductility at room temperature appeared at a scanning rate of 1.1 m/s (see Hardness of 536 HV, compressive strength of 2085 MPa, and DBF of 21.76 %), moreover, remaining a considerable thermal resistance (compressive strength of 738 MPa) at 1200 °C. Furthermore, the methodology and mechanism of the cracking suppression as well as enhancement of the mechanical properties of the matrix are applicable to guiding the future development of the additively manufactured WMoTaNb and WMoTaNb-based RHEAs.

## CRediT authorship contribution statement

**Bang Xiao:** Writing – review & editing, Writing – original draft, Supervision, Methodology, Investigation, Formal analysis, Conceptualization. **Fangzhou Xing:** Formal analysis, Software. **Wenpeng Jia:** Formal analysis, Funding acquisition, Investigation, Methodology, Project administration. **Jian Wang:** Formal analysis, Funding acquisition, Investigation, Project administration, Writing – review & editing. **Ming Wei:** Formal analysis, Investigation, Methodology, Software, Writing – review & editing. **Lian Zhou:** Methodology, Supervision.

## Declaration of competing interest

The authors declare that they have no known competing financial interests or personal relationships that could have appeared to influence the work reported in this paper.

## Data availability

No data was used for the research described in the article.

## Acknowledgment

We authors thank the State Key Laboratory of Porous Metal Materials of the Northwest Institute for Non-ferrous Metal Research (China) for providing funding.

## References

- [1] C. Zhu, Z.P. Lu, T.G. Nieh, Incipient plasticity and dislocation nucleation of FeCoCrNiMn high-entropy alloy, *Acta Mater.* 61 (2013) 2993–3001.
- [2] O.N. Senkov, D.B. Miracle, K.J. Chaput, J.P. Cousinie, Development and exploration of refractory high entropy alloys-A review, *J. Mater. Res.* 33 (2018) 3092–3128.
- [3] P.N. Browning, S. Alagic, A. Kulkarni, L. Matson, J. Singh, Room and ultrahigh temperature structure-mechanical property relationships of tungsten alloys formed by field assisted sintering technique (FAST), *Mater. Sci. Eng., A* 674 (2016) 701–712.
- [4] A. Kohyama, N. Igata, Mechanical properties of electron beam welded molybdenum alloys, *J. Nucl. Mater.* 122 (1984) 767–771.
- [5] M.G. Poletti, G. Fiore, F. Gili, D. Mangherini, L. Battezzati, Development of a new high entropy alloy for wear resistance: FeCoCrNiW<sub>0.3</sub> and FeCoCrNiW<sub>0.3</sub>+5 at.% of C, *Mater. Des.* 115 (2017) 247–254.
- [6] J.W. Wang, Y. Liu, B. Liu, Y. Wang, Y.K. Cao, T.C. Li, R. Zhou, Flow behavior and microstructures of powder metallurgical CrFeCoNiMo<sub>0.2</sub> high entropy alloy during high temperature deformation, *Mater. Sci. Eng., A* 689 (2017) 233–242.
- [7] W.Y. Huo, H. Zhou, F. Fang, X.F. Zhou, Z.H. Xie, J.Q. Jiang, Microstructure and properties of novel CoCrFeNiTa<sub>x</sub> eutectic high-entropy alloys, *J. Alloys Compd.* 735 (2018) 897–904.
- [8] W.H. Liu, J.Y. He, H.L. Huang, H. Wang, Z.P. Lu, C.T. Liu, Effects of Nb additions on the microstructure and mechanical property of CoCrFeNi high-entropy alloys, *Intermetallics* 60 (2015) 1–8.
- [9] H. Tan, T.T. Hu, F.Y. Zhang, Y. Qiu, A.T. Clare, Direct metal deposition of satellite Ti-15Mo: microstructure and mechanical properties, *Adv. Eng. Mater.* (2019) 1900152.
- [10] M.Y. Mendoza, P. Samimi, D.A. Brice, B.W. Martin, M.R. Rolchigo, R. Lesar, P. C. Collins, Microstructure and grain refinement of additive-manufactured Ti-xW alloys, *Mater. Trans. A* 48A (2017) 3594–3605.
- [11] O.N. Senkov, G.B. Wilks, J.M. Scott, D.B. Miracle, Mechanical properties of Nb<sub>25</sub>Mo<sub>25</sub>Ta<sub>25</sub>W<sub>25</sub> and V<sub>20</sub>Nb<sub>20</sub>Mo<sub>20</sub>Ta<sub>20</sub>W<sub>20</sub> refractory high entropy alloys, *Intermetallics* 19 (2011) 698–706.
- [12] Z.Q. Wang, H.H. Wu, Y. Wu, H.L. Huang, X.Y. Zhu, Y.J. Zhang, H.H. Zhu, X. Y. Yuan, Q. Chen, S.D. Wang, X.J. Liu, H. Wang, S.H. Jiang, M.J. Kim, Z.P. Lu, Solving oxygen embrittlement of refractory high-entropy alloy via grain boundary engineering, *Mater. Today* 54 (2022) 83–89.
- [13] L. Qi, D.C. Chrzan, Tuning ideal tensile strengths and intrinsic ductility of bcc refractory alloys, *Phys. Rev. Lett.* 112 (2014) 115503.
- [14] A.H. Cottrell, Strengths of grain boundaries in pure metals, *Mater. Sci. Technol.* 5 (1989) 1165–1167.
- [15] N.H. Macmillan, A. Kelly, The mechanical properties of perfect crystals. II. The stability and mode of fracture of highly stressed ideal crystals, *Proc. Roy. Soc. Lond. A* 330 (1972) 309–317.
- [16] D.B. Miracle, O.N. Senkov, A critical review of high entropy alloys and related concepts, *Acta Mater.* 122 (2017) 448–511.
- [17] Z.D. Han, N. Chen, S.F. Zhao, L.W. Fan, G.N. Yang, Y. Shao, K.F. Yao, Effect of Ti additions on mechanical properties of NbMoTaW and VNbMoTaW refractory high entropy alloys, *Intermetallics* 84 (2017) 153–157.
- [18] Y.G. Tong, L.H. Bai, X.B. Liang, Y.X. Chen, Z.B. Zhang, J. Liu, Y.J. Li, Y.L. Hu, Influence of alloying elements on mechanical and electronic properties of NbMoTaWX (X = Cr, Zr, V, Hf and Re) refractory high entropy alloys, *Intermetallics* 126 (2020) 106928.
- [19] Z.D. Han, H.W. Luan, X. Liu, N. Chen, X.Y. Li, Y. Shao, K.F. Yao, Microstructures and mechanical properties of Ti<sub>x</sub>NbMoTaW refractory high-entropy alloys, *Mater. Sci. Eng., A* 712 (2018) 380–385.
- [20] S. Guo, C. Ng, J. Lu, C.T. Liu, Effect of valence electron concentration on stability of fcc or bcc phase in high entropy alloys, *J. Appl. Phys.* 109 (2011) 103505.
- [21] S.Y. Wu, D.X. Qiao, H.L. Zhao, J. Wang, Y.P. Lu, A novel NbTaW<sub>0.5</sub>(Mo<sub>2</sub>O<sub>x</sub>) refractory high-entropy alloy with excellent mechanical properties, *J. Alloys Compd.* 889 (2021) 161800.
- [22] A. Roh, D.Y. Kim, S.J. Nam, D.I. Kim, H.Y. Kim, K.A. Lee, H.J. Choi, J.H. Kim, NbMoTaW refractory high entropy alloy composites strengthened by in-situ metal-non-metal compounds, *J. Alloys Compd.* 822 (2020) 153423.
- [23] J.H. Westbrook, Segregation at grain boundaries, *Metall. Rev.* 9 (1964) 415–471.
- [24] M. Wu, Z.M. Li, B. Gault, P. Munroe, I. Baker, The effects of carbon on the phase stability and mechanical properties of heat-treated FeNiMnCrAl high entropy alloys, *Mater. Sci. Eng., A* 748 (2019) 59–73.
- [25] S.L. Wei, S.J. Kim, J.Y. Kang, Y. Zhang, Y.J. Zhang, T. Furuhara, E.S. Park, C. C. Tasan, Natural-mixing guided design of refractory high-entropy alloys with as-cast tensile ductility, *Nat. Mater.* 19 (2020) 1175–1181.
- [26] Y. Long, X.B. Liang, K. Su, H.Y. Peng, X.Z. Li, A fine-grained NbMoTaWVCr refractory high-entropy alloy with ultra-high strength: microstructural evolution and mechanical properties, *J. Alloys Compd.* 780 (2019) 607–617.
- [27] W.C. Wei, T. Wang, C.Y. Wang, M. Wu, Y.P. Nie, J. Peng, Ductile W<sub>0.4</sub>MoNb<sub>x</sub>TaTi refractory high-entropy alloys with excellent elevated temperature strength, *Mater. Lett.* 295 (2021) 129753.

- [28] O.N. Senkov, G.B. Wilks, D.B. Miracle, C.P. Chuang, P.K. Liaw, Refractory high-entropy alloys, *Intermetallics* 18 (2010) 1758–1765.
- [29] A. Poulia, E. Georgatis, A. Lekatou, A.E. Karantzalis, Microstructure and wear behavior of a refractory high entropy alloy, *Int. J. Refract. Met. H.* 57 (2016) 50–63.
- [30] S.H. Chen, J.S. Zhang, S. Guan, T. Li, J.Q. Liu, F.F. Wu, Y.C. Wu, Microstructure and mechanical properties of WN<sub>x</sub>MoTaZr<sub>x</sub> (x = 0.1, 0.3, 0.5, 1.0) refractory high entropy alloys, *Mater. Sci. Eng., A* 835 (2022) 142701.
- [31] H. Doppelstein, E.P. George, E.L. Gurevich, A. Kostka, A. Ostendorf, G. Laplanche, Laser metal deposition of refractory high-entropy alloys for high-throughput synthesis and structure-property characterization, *Int. J. Extrem. Manuf.* 3 (2021) 015201.
- [32] H. Zhang, Y.Z. Zhao, J.L. Cai, S.K. Ji, J.L. Geng, X.Y. Sun, D.C. Li, High-strength NbMoTaX refractory high-entropy alloy with low stacking fault energy eutectic phase via laser additive manufacturing, *Mater. Des.* 201 (2021) 109462.
- [33] C.J. Han, Q.H. Fang, Y.S. Shi, S.B. Tor, C.K. Chua, K. Zhou, Recent advances on high-entropy alloys for 3D printing, *Adv. Mater.* (2020) 1903855.
- [34] A.O. Moghaddama, N.A. Shaburova, M.N. Samodurova, A. Abdollahzadeh, E. A. Trofimov, Additive manufacturing of high entropy alloys: a practical review, *J. Mater. Sci. Technol.* 77 (2021) 131–162.
- [35] T. DebRoy, H.L. Wei, J.S. Zuback, T. Mukherjee, J.W. Elmer, J.O. Milewski, A. M. Beese, A. Wilson-Heid, A. De, W. Zhang, Additive manufacturing of metallic components-Process, structure and properties, *Prog. Mater. Sci.* 92 (2018) 112–224.
- [36] H. Doppelstein, M. Thiele, E.L. Gurevich, E.P. George, A. Ostendorf, Direct metal deposition of refractory high-entropy alloy MoNbTaW, *Phys. Procedia* 83 (2016) 624–633.
- [37] M.A. Melia, S.R. Whetten, R. Puckett, M. Jones, M.J. Heiden, N. Argibay, A. B. Kustas, High-throughput additive manufacturing and characterization of refractory high entropy alloys, *Appl. Mater. Today* 19 (2020) 100560.
- [38] P.F. Gu, T.B. Qi, L. Chen, T. Ge, X.D. Ren, Manufacturing and analysis of VN<sub>x</sub>MoTaW refractory high-entropy alloy fabricated by selective laser melting, *Int. J. Refract. Met. H.* 105 (2022) 105834.
- [39] S. Kou, A criterion for cracking during solidification, *Acta Mater.* 88 (2015) 366–374.
- [40] B. Xiao, W.P. Jia, H.P. Tang, J. Wang, L. Zhou, Microstructure and mechanical properties of WMoTaNbTi refractory high-entropy alloys fabricated by selective electron beam melting, *J. Mater. Sci. Technol.* 108 (2022) 54–63.
- [41] S. Shiva, I.A. Palani, S.K. Mishra, C.P. Paul, L.M. Kukreja, Investigations on the influence of composition in the development of Ni-Ti shape memory alloy using laser based additive manufacturing, *Opt. Laser. Technol.* 69 (2015) 44–51.
- [42] S.F. Liu, W. Liu, J.B. Liu, J. Liu, L. Zhang, Y.J. Tang, L.C. Zhang, L.Q. Wan, Compressive properties and microstructure evolution in NiTiNb alloy with mesh eutectic phase, *Mater. Sci. Eng., A* 801 (2021) 140434.
- [43] P.L. Raffo, Yielding and fracture in tungsten and tungsten-rhenium alloys, *J. Less Common. Met.* 17 (1969) 133–149.
- [44] A. Xu, D.E.J. Armstrong, C. Beck, M.P. Moody, G.D.W. Smith, P.A.J. Bagot, S. G. Roberts, Ion-irradiation induced clustering in W-Re-Ta, W-Re and W-Ta alloys: an atom probe tomography and nanoindentation study, *Acta Mater.* 124 (2017) 71–78.
- [45] H.W. Yao, J.W. Qiao, M.C. Gao, J.A. Hawk, S.G. Ma, H.F. Zhou, Y. Zhang, NbTaV<sub>(Ti,W)</sub> refractory high-entropy alloys: experiments and modeling, *Mater. Sci. Eng., A* 674 (2016) 203–211.
- [46] Q.Y. Li, H. Zhang, D.C. Li, Z.H. Chen, S. Huang, Z.L. Lu, H.Q. Yan, W<sub>x</sub>NbMoTa refractory high-entropy alloys fabricated by laser cladding deposition, *Materials* 12 (2019) 533.
- [47] D.Z. Wang, C.F. Yu, J. Ma, W. Liu, Z.J. Shen, Densification and crack suppression in selective laser melting of pure molybdenum, *Mater. Des.* 129 (2017) 44–52.
- [48] H.L. Brown, C.P. Kempster, Elastic properties of thoriated W-Mo and W-Mo-Re alloys, *J. Less Common. Met.* 12 (1967) 166–168.
- [49] S. Wurster, B. Gludovatz, A. Hoffmann, R. Pippan, Fracture behavior of tungsten-vanadium and tungsten-tantalum alloys and composites, *J. Nucl. Mater.* 413 (2011) 166–176.
- [50] T. Mukherjee, J.S. Zuback, A. De, T. DebRoy, Printability of alloys for additive manufacturing, *Sci. Rep.* 6 (2016) 19717.
- [51] O.A. Idowu, O.A. Ojo, M.C. Chaturvedi, Effect of heat input on heat affected zone cracking in laser welded ATI Allvac 718Plus superalloy, *Mater. Sci. Eng., A* 454–455 (2007) 389–397.
- [52] Y.L. Hu, X. Lin, K. Song, X.Y. Jiang, H.O. Yang, W.D. Huang, Effect of heat input on cracking in laser solid formed DZ4125 superalloy, *Opt. Laser. Technol.* 86 (2016) 1–7.
- [53] T. Grábeč, P. Sedláček, K. Zoubková, M. Ševčík, M. Janovská, P. Stoklasová, H. Seiner, Evolution of elastic constants of the NiTi shape memory alloy during a stress-induced martensitic transformation, *Acta Mater.* 208 (2021) 116718.
- [54] B.A. Bimber, R.F. Hamilton, J. Keist, T.A. Palmer, Anisotropic microstructure and superelasticity of additive manufactured NiTi alloy bulk builds using laser directed energy deposition, *Mater. Sci. Eng., A* 674 (2016) 125–134.
- [55] H. Shi, J. Frenzel, G.T. Martinez, S. Van Rompaey, D. Schryvers, Site occupation of Nb atoms in ternary Ni-Ti-Nb shape memory alloys, *Acta Mater.* 74 (2014) 85–95.
- [56] Y. Chen, H.C. Jiang, L.J. Rong, L. Xiao, X.Q. Zhao, Mechanical behavior in NiTiNb shape memory alloys with low Nb content, *Intermetallics* 19 (2011) 217–220.
- [57] Y. Shao, F.M. Guo, Y. Huan, D.Q. Jiang, J.S. Zhang, Y. Ren, L.S. Cui, Fabrication, microstructure and mechanical properties of W-NiTi composites, *J. Alloys Compd.* 695 (2017) 1976–1983.
- [58] J. Van Humbeeck, Damping capacity of thermoelastic martensite in shape memory alloys, *J. Alloys Compd.* 355 (2003) 58–64.
- [59] Z.Z. Bao, S. Guo, F. Xiao, X.Q. Zhao, Development of NiTiNb in-situ composite with high damping capacity and high yield strength, *Prog. Nat. Sci.-Mater.* 21 (2011) 293–300.
- [60] I. Polozov, A. Popovich, Microstructure and mechanical properties of NiTi-based eutectic shape memory alloy produced via selective laser melting in-situ alloying by Nb, *Materials* 14 (2021) 2696.
- [61] S. Saedi, A.S. Turabi, M.T. Andani, C. Haberland, H. Karaca, M. Elahinia, The influence of heat treatment on the thermomechanical response of Ni-rich NiTi alloys manufactured by selective laser melting, *J. Alloys Compd.* 677 (2016) 204–210.
- [62] J. Frenzel, E.P. George, A. Dlouhy, Ch. Somsen, M.F.-X. Wagner, G. Eggeler, Influence of Ni on martensitic phase transformations in NiTi shape memory alloys, *Acta Mater.* 58 (2010) 344–345.
- [63] Q. Zhou, M.D. Hayat, G. Chen, S. Cai, X.H. Qu, H.P. Tang, P. Cao, Selective electron beam melting of NiTi: microstructure, phase transformation and mechanical properties, *Mater. Sci. Eng., A* 744 (2019) 290–298.
- [64] M. Shioiri, K. Osakada, K. Nakamura, T. Yamashita, F. Abe, Residual stress within metallic model made by selective laser melting process, *CIRP Annals* 53 (2004) 195–198.
- [65] H. Zhang, W. Xu, Y.J. Xu, Z.L. Lu, D.C. Li, The thermal-mechanical behavior of Ta<sub>x</sub>MoNb high-entropy alloy via selective laser melting (SLM): experiment and simulation, *Int. J. Adv. Manuf. Technol.* 96 (2018) 461–474.
- [66] F. Xiao, G.J. Ma, X.Q. Zhao, H.B. Xu, Effects of Nb content on yield strength of NiTiNb Alloys in martensite state, *Chin. J. Aeronaut.* 22 (2009) 658–662.
- [67] E. Choi, H.K. Hong, H.S. Kim, Y.S. Chung, Hysteretic behavior of NiTi and NiTiNb SMA wires under recovery or pre-stressing stress, *J. Alloys Compd.* 577 (2013) S444–S447.
- [68] D.B. Williams, C. Barry Carter, *Transmission Electron Microscopy*, Springer, New York, 2009, pp. 451–481.
- [69] A. Luo, K.S. Shin, D.L. Jacobson, Hafnium carbide strengthening in a tungsten-rhenium matrix at ultrahigh temperatures, *Acta Metall. Mater.* 4 (1992) 2225–2232.
- [70] R.K. Gupta, V. Anil Kumar, Arjun Sukumaran, V. Kumar, High-temperature tensile behaviors of base metal and electron beam-welded joints of Ni-20Cr-9Mo-4Nb superalloy, *Metall. Mater. Trans. A* 49 (2018) 2654–2672.
- [71] B. Kombaiah, K.L. Murty, Coble, Orowan strengthening, and dislocation climb mechanisms in a Nb-modified zircaloy cladding, *Metall. Mater. Trans. A* 46A (2015) 4646–4660.
- [72] K.L. Li, G.Q. Ma, L.L. Xing, Y.F. Wang, C.F. Yu, J.H. Chen, J. Ma, G.L. Wu, W. Liu, Z.J. Shen, X.X. Huang, Crack suppression via in-situ oxidation in additively manufactured W-Ta alloy, *Mater. Lett.* 263 (2020) 127212.
- [73] M.C. Carroll, L.J. Carroll, Developing dislocation subgrain structures and cyclic softening during high-temperature creep-fatigue of a nickel alloy, *Metall. Mater. Trans. A* 44A (2013) 3592–3607.
- [74] N.A. Ley, S. Segovia, S. Gorsse, M. Young, Characterization and modeling of NbNiTaTiW and NbNiTaTiW-Al refractory high-entropy alloys, *Metall. Mater. Trans. A* 50 (2019) 4867–4876.
- [75] M.S. Dodarad, S.M. Guo, M.M. Khonsari, N. Shamsaei, S. Shao, A theoretical calculation of stacking fault energy of Ni alloys: the effects of temperature and composition, *Comput. Mater. Sci.* 191 (2021) 110326.
- [76] T.Z. Khan, T. Kirk, G. Vazquez, P. Singh, A.V. Smirnov, D.D. Johnson, K. Youssef, R. Arróyave, Towards stacking fault energy engineering in FCC high entropy alloys, *Acta Mater.* 224 (2022) 117472.
- [77] S.P. Murray, K.M. Pusch, A.T. Polonsky, C.J. Torbet, G.G.E. Seward, N. Zhou, S.A. J. Forsik, P. Nandwana, M.M. Kirka, R.R. Dehoff, W.E. Slye, T.M. Pollock, A defect-resistant Co-Ni superalloy for 3D printing, *Nat. Commun.* 11 (2020) 4975.
- [78] V. Juechter, T. Scharowsky, R.F. Singer, C. Körner, Processing window and evaporation phenomena for Ti-6Al-4V produced by selective electron beam melting, *Acta Mater.* 76 (2014) 252–258.
- [79] H. Mughrabi, Dual role of deformation-induced geometrically necessary dislocations with respect to lattice plane misorientations and/or long-range internal stresses, *Acta Mater.* 54 (2006) 3417–3427.
- [80] D. Kong, C. Dong, X. Ni, Z. Liang, C. Man, X. Li, Hetero-deformation-induced stress in additively manufactured 316L stainless steel, *Mater. Res. Lett.* 8 (10) (2020) 390–397.
- [81] Y.J. Hong, C.S. Zhou, Y.Y. Zheng, L. Zhang, J.Y. Zheng, X.Y. Chen, B. An, Formation of strain-induced martensite in selective laser melting austenitic stainless steel, *Mater. Sci. Eng., A* 740 (2019) 420–426.
- [82] D.C. Kong, C.F. Dong, S.L. Wei, X.Q. Ni, L. Zhang, R.X. Li, L. Wang, C. Man, X. G. Li, About metastable cellular structure in additively manufactured austenitic stainless steels, *Addit. Manuf.* 38 (2021) 101804.
- [83] D.Y. Lin, L.Y. Xu, Y.D. Han, Y.K. Zhang, H.Y. Jing, L. Zhao, F. Minami, Structure and mechanical properties of a FeCoCrNi high-entropy alloy fabricated via selective laser melting, *Intermetallics* 127 (2020) 106963.
- [84] Y.M. Wang, T. Voisin, J.T. McKeown, J.C. Ye, N.P. Calta, Zan Li, Z. Zeng, Y. Zhang, W. Chen, T.T. Roehling, R.T. Ott, M.K. Santala, P.J. Depond, M. J. Matthews, A.V. Hamza, T. Zhu, Additively manufactured hierarchical stainless steels with high strength and ductility, *Nat. Mater.* 17 (2018) 63–71.
- [85] I. Todd, Printing steels, *Nat. Mater.* 17 (2018) 13–14.
- [86] C. Lee, Y. Chou, G. Kim, M.C. Gao, K. An, J. Brechtl, C. Zhang, W. Chen, J. D. Poplawsky, G. Song, Y. Ren, Y.C. Chou, P.K. Liaw, Lattice-distortion-enhanced yield strength in a refractory high-entropy alloy, *Adv. Mater.* 32 (2020) 2004029.

- [87] Z.J. Wang, W.F. Qiu, Y. Yang, C.T. Liu, Atomic-size and lattice-distortion effects in newly developed high-entropy alloys with multiple principal elements, *Intermetallics* 64 (2015) 63–69.
- [88] Z.M. Li, K.G. Pradeep, Y. Deng, D. Raabe, C.C. Tasan, Metastable high-entropy dual-phase alloys overcome the strength-ductility trade-off, *Nature* 534 (2016) 227–230.
- [89] Y.Q. Bu, Y. Wu, Z.F. Lei, X.Y. Yuan, H.H. Wu, X.B. Feng, J.B. Liu, J. Ding, Y. Lu, H. T. Wang, Z.P. Lu, W. Yang, Local chemical fluctuation mediated ductility in body-centered-cubic high-entropy alloys, *Mater. Today* 46 (2021) 28–34.
- [90] B. Chen, S.K. Moon, X. Yao, G. Bi, J. Shen, J. Umeda, K. Kondoh, Strength and strain hardening of a selective laser melted AlSi10Mg alloy, *Scripta Mater.* 141 (2017) 45–49.
- [91] Z.G. Zhu, Q.B. Nguyen, F.L. Ng, X.H. An, X.Z. Liao, P.K. Liaw, S.M.L. Nai, J. Wei, Hierarchical microstructure and strengthening mechanisms of a CoCrFeNiMn high entropy alloy additively manufactured by selective laser melting, *Scripta Mater.* 154 (2018) 20–24.
- [92] J.D. Eshelby, F.C. Frank, F.R.N. Nabarro, The equilibrium of linear arrays of dislocations, *Philos. Mag. A* 42 (1951) 351–364.
- [93] S. Kondo, T. Mitsuma, N. Shibata, Y. Ikuhara, Direct observation of individual dislocation interaction processes with grain boundaries, *Sci. Adv.* 2 (2016) e1501926.
- [94] E.M. Schulson, T.M. Weihs, I. Baker, H.J. Frost, J.A. Horton, Grain boundary accommodation of slip in Ni<sub>3</sub>Al containing boron, *Acta Metall.* 34 (1986) 1395–1399.
- [95] I. Baker, E.M. Schulson, J.A. Horton, In-situ straining of Ni<sub>3</sub>Al in a transmission electron microscope, *Acta Metall.* 35 (1987) 1533–1541.
- [96] I.M. Robertson, T.C. Lee, R. Subramanian, H.K. Birnbaum, The effect of grain boundary chemistry on the slip transmission process through grain boundaries in Ni<sub>3</sub>Al, *MRS Proceedings* 238 (1991) 357–367.
- [97] W.L. Ren, J.T. Guo, G.S. Li, J.Y. Zhou, The role of Nd solid-solution and grain-boundary segregation in binary NiAl intermetallic compound, *J. Mater. Sci. Technol.* 20 (2004) 163–166.
- [98] X.R. Qian, Y.T. Chou, Grain boundary softening in boron-doped Ni<sub>3</sub>Al, *MRS Proceedings* 122 (1988) 311–316.
- [99] S.W. McAlpine, J.V. Logan, M.P. Short, Predicting single phase stability and segregation in the NbMoTaTi-(W, V) high entropy alloy system with the vacancy exchange potential, *Scripta Mater.* 191 (2021) 29–33.
- [100] J.Y. Pan, T. Dai, T. Lu, X.Y. Ni, J.W. Dai, M. Li, Microstructure and mechanical properties of Nb<sub>25</sub>Mo<sub>25</sub>Ta<sub>25</sub>W<sub>25</sub> and Ti<sub>8</sub>Nb<sub>23</sub>Mo<sub>23</sub>Ta<sub>23</sub>W<sub>23</sub> high entropy alloys prepared by mechanical alloying and spark plasma sintering, *Mater. Sci. Eng., A* 738 (2018) 362–366.
- [101] O.A. Waseem, J. Lee, H.M. Lee, H.J. Ryu, The effect of Ti on the sintering and mechanical properties of refractory high-entropy alloy Ti<sub>x</sub>WTaVCr fabricated via spark plasma sintering for fusion plasma-facing materials, *Mater. Chem. Phys.* 210 (2018) 87–94.
- [102] S.W. Liu, H.H. Zhu, G.Y. Peng, J. Yin, X.Y. Zeng, Microstructure prediction of selective laser melting AlSi10Mg using finite element analysis, *Mater. Des.* 142 (2018) 319–328.